Recent human-induced atmospheric drying across Europe unprecedented in the last 400 years

In the format provided by the authors and unedited

Supplementary Information

Table of contents

Supplementary Results and Discussion

Spatial distribution of mean site $\delta^{18}O$ values

Mean $\delta^{18}O$ values (averaged over the period 1900-1994 for each chronology) range from 25.35‰ ('Fur' in Sweden) to 33.48‰ ('Caz' in Southern Spain), representing the geographic location of the sites with a general decrease of $\delta^{18}O$ in both broadleaves and conifers, from the Mediterranean to Fennoscandia and from west to east (Table S1; Fig. S1). Mean $\delta^{18}O$ values of conifers increase from lower to higher elevations opposite to the well-known ^{18}O-depletion of atmospheric moisture with altitude[61]. Since most of the highest-elevation sites are located in the southern part of the network the effect of ^{18}O-enrichment towards lower latitudes dominates the effect of ^{18}O-depletion towards higher elevations. Overall, the observed geographic distribution of $\delta^{18}O$ values mirrors the well-known large-scale patterns of $\delta^{18}O$ values in precipitation and their general dependency on the origin and trajectory of air masses and associated condensation temperatures[62,63]. Species-specific patterns of mean $\delta^{18}O$ values across the network exhibit similar means between broadleaves (28.77‰, SD ± 1.75 ‰) and conifers (28.66‰, SD ± 2.14‰). Therefore, no adjustment is needed in this study as for both groups the effect of geographical location dominates the effect of species, with lowest $\delta^{18}O$ values for both broadleaves and conifers in Fennoscandia (25.49‰ at 'Tur' and 25.35‰ at 'Fur') and highest $\delta^{18}O$ values for both broadleaves and conifers in France and Spain (31.21‰ at 'Fon', and 33.48‰ at 'Caz') (Table S1; Fig. S1).

Response of tree-ring $\delta^{18}O$ to climate variables

Summer conditions (June to August) emerged as the key drivers of tree-ring δ^{18}O variability at most of the climate-sensitive sites across the network, while previous-year conditions were of minor relevance. This finding did not only hold for oak, where mostly latewood was isotopically measured, but also for most sites with other broadleaved species and also for conifers where whole rings (earlywood and latewood together) were measured. Therefore, tree-ring cellulose δ^{18}O does not seem affected by substantial carry-over effects from previous years. Its isotopic signature is mainly created during the peak of meristematic activity and xylem cell-wall thickening in summer[64] if sufficient water transport is provided[26]. Any previous year δ^{18}O signatures potentially conveyed via remobilized reserves may be diluted during starch breakdown where ca. 45% of the old organic oxygen is replaced by oxygen from current water[65].

Climate calibration across two independent periods (1920-1960 and 1961-2000) indicates a slight increase of the correlations between the tree-ring δ^{18}O chronologies and VPD and T_{max} respectively in the modern period at many sites and simultaneously some weakening of the correlations to PPT and SPEI (Fig. S2; Table S2).

Geographic location (i.e. latitude, longitude and altitude) does not have a significant effect on the correlation strength of either broadleaved or coniferous sites to summer VPD and T_{max}, while correlations of the coniferous sites to summer PPT and SPEI significantly increase ($p<0.05$) from South to North (Fig. S3). Also, no significant dependency of the correlation strength to site-dependent long-term means of various climatic variables was found (Fig. S4), except a decrease towards those sites with driest atmospheric summer conditions (highest mean VPD values), i.e. the southernmost,

3

Mediterranean sites (Fig. S4). Relatively weak summer VPD signals also appear at the northwestern edge of the network (northern Scotland and northwest Fennoscandia). Temporal decoupling of leaf phenology and xylem cell development during the growing season, lower transpiration rates and longer turnover times for water in the stem, together with reduced phloem transport may disconnect the tree-ring $\delta^{18}O$ signature of trees in those areas from the immediate influence of summer climate variables.

Sensitivity of tree-ring $\delta^{18}O$ to summer VPD in different European target regions

Tree-ring $\delta^{18}O$ sensitivity to summer VPD was strongest in the temperate lowlands of Europe where evapotranspiration is closely linked with the atmospheric moisture demand[42,43,44], soil moisture is generally not limiting and stomatal conductance (g_s) is relatively high. Since high g_s is partly coupled with VPD-dependent evaporative ^{18}O enrichment in the leaves, the isotopic values of the newly produced assimilates used for cellulose synthesis carry a particularly strong VPD signal[66,67]. This signal is further amplified by a potential link between VPD and precipitation $\delta^{18}O$ as source water for the trees[23,24]. Reduced sensitivity of tree-ring $\delta^{18}O$ to VPD was observed at the northernmost and southernmost edge of the network: In sub-arctic/arctic NF, low atmospheric moisture demand, low temperatures and short growing seasons affect leaf physiology (low transpiration and photosynthesis), together with heterogeneous soil moisture conditions (e.g. varying amount of and access to meltwater from thawing permafrost[68]. In the Mediterranean, a dry atmosphere in summer coupled with low soil moisture availability causes a reduction in g_s and even cessation of cambial activity to minimize water loss via

4

transpiration and avoid critical water tension within the xylem[69]. These effects can be amplified when the topsoil dries out, and trees may access deeper soil water pools that are also decoupled from atmospheric conditions[70].

Comparison with European scale hydroclimatic reconstructions

We here present the first summer VPD reconstructions at the European scale and compare these to existing hydroclimatic reconstructions (Fig. S7). Such comparisons are, however, limited by substantial differences in the moisture characteristics of the target variables.

A few similarities appear with the Old-World Drought Atlas (OWDA)[71] with significant correlations between the unfiltered records ranging from $r_{1600-2000}$=0.23 (AP) to 0.37 (WE) (all $p<0.05$) but no significant correlations in the overall long-term trends, except AP $r_{low-pass1600-2000}$=0.43, $p<0.05$). Comparison with a precipitation reconstruction in Western Europe[72] and a PDSI reconstruction in Eastern Central EuropeB[73] revealed that significant correlations were restricted to the unfiltered records (WE: $r_{1600-2000}$=0.18, $p<0.05$; ECE: $r_{1600-2000}$=0.49; $p<0.01$) but no correlations between the long-term trends were found. A trend to drier conditions at the end of the 20th century is seen in our data, the precipitation and PDSI reconstructions but not in the OWDA. A Central European megadrought during the Dalton Minimum (1770-1840 CE) reported for OWDA based reconstructions[61,74] is not as prominent in our reconstructions.

It is important to consider that specifically in the European temperate lowlands such as WE and ECE hydroclimate reconstructions based on parameters other than pure tree-ring

5

δ^{18}O contain substantial uncertainties. Many of the tree-ring width chronologies included in the OWDA originate from high elevation and boreal sites while drought reconstructions for the temperate lowlands largely depend on less climate sensitive and extrapolated proxy data. Further, our δ^{18}O-based records are less biased by non-climatic long-term trends compared to the other reconstructions (see main text). Therefore, we suggest that the Dalton Minimum "megadrought" has been overestimated in the OWDA based reconstructions.

Potential links to NAO

Correlations between NAO indices, and observational and reconstructed VPD data (common period of overlap) were comparably strong, and highly significant relationships ($p<0.01$) appeared for all four investigated regions (Table S4). Although the strength of the relationships decreased in the early period of the records, probably due to the decreasing quality of the instrumental data, they nevertheless remained highly significant ($p<0.01$). While WE, ECE and AP were mainly related to winter NAO, SF was exclusively related to summer NAO. A link between winter NAO and summer VPD may partly be explained by the relationship between the amount of winter precipitation and summer moisture availability[77]. However, as outlined in the main text, VPD depends on rather complex ocean-land–atmosphere water exchange mechanisms and recycling processes, i.e., the rate at which vapor is supplied to the atmosphere via both ocean evaporation and land surface evapotranspiration, and the strength of this ocean-land-atmosphere coupling. How these complex mechanisms are in detail related to large-scale ocean-

atmosphere circulation dynamics such as NAO, and how the strength of such relationships varies over time is still a topic of research.

ESM simulations of summer VPD with and without land use/land cover change included

Simulations with LULC change included reveal lower VPD levels than those not considering such change, with larger reductions in Western Europe and in the Alps & Pyrenees compared to Eastern Central Europe and Southern Fennoscandia (Table S8). This means that LULC change partly counteracted the recent increase in VPD. To date, no studies exist from our knowledge on the effect of LULC changes on VPD, and there is no clear consensus in the literature if an increase in heat and drought may be mitigated or exacerbated by LULC change. It has, however, been demonstrated that land-atmosphere feedbacks caused by historical European LULC changes led to widespread changes in the energy and water balances. Reductions in cropland and agricultural abandonment may have substantially increased cloud cover and decreased incoming shortwave radiation in western Europe. The response of the water and energy balances was lessened in areas with shallow groundwater, indicating that local- and continental-scale responses to LULC change are influenced by the coupling between the subsurface, land surface, and atmosphere[78]. Further, there is observational evidence for a strong increase in cloud cover over large forest regions in western Europe, and that widespread windthrow by cyclonic weather systems led to a significant decrease in local cloud cover in subsequent years[79]. This would support a dampening in the VPD increase in line with a change from croplands to shrub and forest areas. Nevertheless, even with the effect of LULC change

included in our simulations, atmospheric drying over Europe during 1991-2020 remains

unprecedented and is clearly driven by human-induced greenhouse gas emissions.

Supplementary References

61. K. Rozanski, L. Araguas-Araguas, R. Gonfiantini, Relation between long-term trends of oxygen-18 isotope composition of precipitation and climate. *Science* **258**, 981–-985 (1992).
62. N. J. Loader *et al*., Summer precipitation for the England and Wales region, 1201–2000 CE, from stable oxygen isotopes in oak tree rings. *J. Quat. Sci.* **35**, 731-736 (2021). K. Treydte *et al*., Seasonal transfer of oxygen isotopes from precipitation and soil to the tree ring: Source water versus leaf water enrichment. *New Phytol.* **202***, 772-783 (2014).
63. D. F. Balting *et al.,* Large-scale climate signals of a European oxygen isotope network from tree rings, *Clim. Past* **17**, 1005–1023 (2020).
64. H. Cuny *et al.,* Woody biomass production lags stem-girth increase by over one month in coniferous forests. *Nat. Plants* **1,** 15160 (2015).
65. A. Gessler, A. D. Peuke, C. Keitel, G. D. Farquhar, Oxygen isotope enrichment of organic matter in Ricinus communis during the diel course and as affected by assimilate transport. *New Phytol.* **174**, 600-613 (2007).
66. Kahmen, A. *et al.,* Cellulose δ^{18}O is an index of leaf-to-air vapor pressure difference (VPD) in tropical plants. *Proc. Nat. Ac. Sci*. **108**, 1981–1986 (2011).
67. Lehmann, M. M., Gamarra, B., Kahmen, A., Siegwolf, R. T. W., Saurer, M. Oxygen isotope fractionations across individual leaf carbohydrates in grass and tree species. *Plant Cell Environ.* **40**, 1658–1670 (2017).
68. Churakova Sidorova, O. V. *et al.,* Recent atmospheric drying in Siberia is not unprecedented over the last 1,500 years *Sci. Rep.* **10**, 15024 (2020).
69. Running, S. Environmental control of leaf water conductance in conifers. *Can. J. For. Res.* **6**, https://doi.org/10.1139/x76-013 (1976).
70. Sarris, D., Siegwolf, R. T. W., Körner, C. Inter- and intra-annual stable carbon and oxygen isotope signals in response to drought in Mediterranean pines. *Agr. For. Meteor.* **168**, 59-68 (2013).
71. Cook, E. R. et al. Old World megadroughts and pluvials during the Common Era. *Sci. Adv* **1**, https://doi.org/10.1126/sciadv.1500561 (2015).
72. Büntgen, U. *et al.,* 2500 years of European climate variability and human susceptibility. *Science* **331**, 578–582 (2011).
73. Büntgen, U. *et al.,* Recent European drought extremes beyond Common Era background variability. *Nature Geoscience* https://doi.org/10.1038/s41561-021-00698-0 (2021).
74. Ionita, M., Dima, M., Nagavciuc, V., Scholz, P., Lohmann, G. Past megaodroughts in central Europe were longer, more severe and less warm than modern droughts.

Nature Comm. Earth Environ. **2,** https://doi.org/10.1038/s43247-021-00130-w (2021).

75. Trenberth, K. E. and Paolino, D. A. The Northern Hemisphere sea level pressure data set: Trends, errors, and discontinuities. *Mon. Wea. Rev.* **108**, 855-872 (1980).

76. Jones, P.D., Jónsson, T., Wheeler, D. Extension to the North Atlantic Oscillation using early instrumental pressure observations from Gibraltar and South-West Iceland. *Int. J. Climatol.* **17**, 1433-1450 (1997).

77. Quesada, B. *et al.,* Asymmetric European summer heat predicatbility from wet and dry southern winter and springs. *Nat. Clim. Change*. **2**, 736-741 (2013).

78. Zipper, S. C. *et al.,* Land use change impacts on European heat and drought : Remote land-atmospher feedbacks mitigated locally by shallow groundwater. *Env. Res. Lett.* **14**, 044012, https://doi.org/10.1088/1748-9326/ab0db3 (2019).

79. Teuling, A. J. *et al.,* Observational evidence for cloud cover enhancement over western European forests. *Nat. Comm.* **8**, 14065, https://doi.org/10.1038/ncomms14065 (2017).

Supplementary Tables

Supplementary Table 1. Summary statistics of the correlation heatmaps in Fig. 2. 'mean r' is the mean of all correlations of the months June, July and August, 'max r' is the overall maximum correlation (in all cases this is found in June, July or August), 'no. JJA p<0.05' is the number of significant correlations at p<0.05 in the months June, July and August, and 'no. all p<0.05' is the number of significant correlations of all months. 'full', 'early' and 'late' are the investigated time periods 1920-2000, 1920-1960 and 1961-2000 respectively.

Variable	mean r JJA	max r	no. JJA p<0.05	no. all p<0.05
VPD full	0.27	0.72	89	195
VPD early	0.23	0.75	49	103
VPD late	0.32	0.74	69	141
Tmax full	0.27	0.67	85	194
Tmax early	0.27	0.75	57	109
Tmax late	0.29	0.70	66	141
PPT full	-0.22	-0.54	78	140
PPT early	-0.25	-0.78	50	97
PPT late	-0.21	-0.57	42	78
SPEI full	-0.23	-0.52	78	141
SPEI early	-0.25	-0.77	53	101
SPEI late	-0.22	-0.61	45	81

Supplementary Table 2. Calibration and verification statistics of the individual PC1 nests for each European region. R^2 = explained variance between nest PC1 score and the JJA VPD data. RE is reduction of error, CE is coefficient of efficiency, LINr P-value is the p-value significance assessment of any linear trend in the model residuals, and DW is Durbin-Watson test. Grey highlighted values are those not significant at the 95% confidence limit.

Region	Nest	Calibration: 1920-1960	Validation: 1961-1994			Full Calibration: 1920-1994		
		R^2	R^2	RE	CE	R^2	LINr P-value	DW
Northern Fennoscandia	1900-2001	0.35	0.36	-0.24	-0.24	0.23	<0.05	1.68
	1620-2001	0.34	0.26	-0.05	-0.06	0.24	<0.05	1.72
	1600-2001	0.33	0.22	-0.05	-0.06	0.22	<0.05	1.76
Southern Fennoscandia	1901-1994	0.27	0.59	0.56	0.55	0.44	0.23	1.80
	1900-1994	0.22	0.53	0.47	0.46	0.37	0.10	1.84
	1736-2002	0.22	0.49	0.43	0.42	0.35	0.06	1.88
	1600-2002	0.21	0.42	0.40	0.39	0.32	0.09	2.01
Western Europe	1900-1994	0.61	0.71	0.63	0.63	0.63	0.50	1.81
	1763-1998	0.62	0.72	0.64	0.64	0.64	0.45	1.91
	1751-1998	0.61	0.69	0.62	0.62	0.63	0.63	1.85
	1749-2000	0.60	0.70	0.64	0.64	0.62	0.82	1.85
	1604-2000	0.52	0.67	0.64	0.64	0.56	0.73	1.81
Eastern Central Europe	1900-2003	0.45	0.53	0.45	0.36	0.52	0.17	1.59
	1850-2003	0.48	0.55	0.39	0.30	0.47	0.07	1.60
	1821-2003	0.48	0.54	0.40	0.30	0.47	0.09	1.56
	1600-2003	0.26	0.42	0.07	-0.08	0.24	<0.05	1.13
Alps & Pyrenees	1901-2003	0.43	0.42	0.39	0.39	0.41	0.15	1.32
	1853-2003	0.45	0.42	0.37	0.37	0.41	0.26	1.34
	1840-2003	0.38	0.34	0.32	0.32	0.35	0.07	1.31
	1783-2003	0.31	0.33	0.31	0.31	0.31	0.08	1.35
	1600-2003	0.25	0.38	0.30	0.30	0.31	<0.05	1.39

Supplementary Table 3. Correlations of regional summer VPD observations and reconstructions to several North Atlantic Oscillation indices for winter (JFM, mean of January/February/March) and summer (JJA, mean of June/July/August). Calculations were performed for the common period of overlap of the reconstructions and observations back to 1950, 1901 and 1824 respectively. Blue (JFM) and red (JJA) bold numbers indicate p<0.01, blue and red regular numbers p<0.05.
NCEP/NCAR: https://www.psl.noaa.gov/data/gridded/data.ncep.reanalysis.html),
UCAR: Summer NAO index (rda.ucar.edu/datasets/ds010.1/)[75];
CPC: NOAA, National Service Climate Prediction Center:
https://www.cpc.ncep.noaa.gov/products/precip/CWlink/pna/nao.shtml);
CRU: Climate Research Unit NAO index[76].

		NCEP/NCAR 1950		UCAR 1950		UCAR 1901			
	Region	JFM	JJA	JFM	JJA	JFM	JJA		
Summer VPD Observations	SF	0.01	**0.47**	0.00	**0.45**	-0.09	**0.47**		
	WE	0.23	**0.45**	0.22	**0.41**	0.25	**0.32**		
	ECE	0.08	-0.13	0.04	-0.18	0.11	-0.15		
	AP	0.20	0.13	0.17	0.07	0.19	0.10		
		CPC 1950		CRU 1950		CRU 1901			
	Region	JFM	JJA	JFM	JJA	JFM	JJA		
	SF	0.22	**0.46**	0.18	-0.04	-0.04	-0.02		
	WE	**0.53**	**0.38**	**0.51**	0.25	0.18	0.07		
	ECE	**0.34**	-0.02	**0.36**	-0.08	0.18	-0.03		
	AP	**0.49**	0.17	**0.42**	0.08	**0.21**	0.02		
		NCEP/NCAR 1950		UCAR 1950		UCAR 1901			
	Region	JFM	JJA	JFM	JJA	JFM	JJA		
Summer VPD Reconstructions	SF	0.21	**0.49**	0.21	**0.50**	0.11	**0.44**		
	WE	**0.29**	**0.52**	**0.26**	**0.49**	**0.28**	**0.41**		
	ECE	0.13	-0.19	0.14	-0.24	**0.21**	-0.23		
	AP	0.20	-0.09	0.15	-0.19	**0.28**	-0.07		
		CPC 1950		CRU 1950		CRU 1901		CRU 1824	
	Region	JFM	JJA	JFM	JJA	JFM	JJA	JFM	JJA
	SF	0.14	**0.41**	0.13	0.03	0.04	0.04	0.12	0.09
	WE	**0.61**	**0.41**	**0.58**	0.27	**0.34**	0.13	**0.25**	0.08
	ECE	**0.32**	-0.07	**0.46**	0.17	**0.26**	0.11	**0.26**	0.04
	AP	**0.27**	0.01	**0.32**	0.20	**0.28**	0.08	**0.23**	0.02

Supplementary Table 4. Comparison of normalized VPD during the period 1991-2020 between simulations excluding human-induced forcing ("hist-nat") and simulations including all forcings ("historical"). Values are provided for the 6 models available and over the regions Southern Fennoscandia (SF), Western Europe (WE), Eastern Central Europe (ECE) and Alps & Pyrenees (AP). Note that for CESM2 the "hist-nat" simulation ends in 2014 instead of 2020.

| Models	"hist-nat" simulations				"historical" simulations			
	SF	WE	ECE	AP	SF	WE	ECE	AP
ACCESS-ESM1-5	-0.05	-0.07	-0.06	-0.13	0.64	0.55	0.61	1.09
CESM2[*]	-0.14	0	0.36	0.06	0.56	0.39	0.69	1.09
CanESM5	-0.16	-0.05	0.19	0.11	1.18	1.51	1.09	1.77
GFDL-ESM4	0.05	0.05	0.17	0.17	-0.29	-0.04	-0.09	0.34
IPSL-CM6A-LR	0.05	-0.05	0.06	0.03	1.17	1.41	0.73	2.31
MRI-ESM2-0	-0.2	0.14	0.13	0.18	-0.01	0.36	0.1	0.54
Multi-model mean	-0.08	0.002	0.14	0.07	0.54	0.7	0.52	1.19

Supplementary Table 5. Interannual standard deviation of summer VPD during the pre-industrial period for the reconstructions and individual model simulations. For the reconstructions this corresponds to 1600 to 1849 CE, whereas for the models all 500 years of the "piControl" simulations were used.

|	SF	WE	ECE	AP
Reconstruction	0.6	0.79	0.83	0.65
ACCESS-ESM1-5	1.16	1.14	1.7	0.99
CESM2	0.99	0.81	1.14	0.52
CMCC-ESM2	1.41	1.12	1.74	0.61
CNRM-ESM2-1	0.94	1.01	1.6	0.99
CanESM5	0.9	0.66	0.92	0.33
EC-Earth3-Veg	1.35	1.19	1.73	0.69
GFDL-ESM4	0.9	0.51	0.81	0.38
IPSL-CM6A-LR	0.74	0.66	1.04	0.65
MIROC-ES2L	1.12	0.84	1.05	0.67
MPI-ESM1-2-LR	1.12	0.82	1.67	0.43
MRI-ESM2-0	1.05	0.61	0.67	0.29
UKESM1-0-LL	0.84	0.81	1.19	0.57

Supplementary Table 6. Comparison of normalized VPD during the period 1991-2014 between simulations with land use/Land cover (LULC) held constant at pre-industrial conditions ("hist-noLu") and simulations including all forcings ("historical"). Here we use data until 2014 because no data are available for the "hist-noLu" simulations up to 2020. Values are provided for the 10 models available and over the regions Southern Fennoscandia (SF), Western Europe (WE), Eastern Central Europe (ECE) and Alps & Pyrenees (AP).

| Models	"hist-noLu" simulations				"historical" simulations			
	SF	WE	ECE	AP	SF	WE	ECE	AP
ACCESS-ESM1-5	0.86	0.55	0.37	0.64	0.36	0.31	0.28	0.87
CESM2	0.52	1.22	0.39	1.84	0.34	0.25	0.46	0.95
CMCC-ESM2	1.52	1.44	1.62	2.3	1.8	1.41	1.3	2.06
CNRM-ESM2-1	0.13	0.63	0.14	0.99	0.16	0.68	-0.23	0.98
CanESM5	0.83	1.92	1.65	2.51	1.2	1.46	1.03	1.55
EC-Earth3-Veg	0.31	0.96	0.34	1.59	-0.12	-0.12	-0.05	0.52
IPSL-CM6A-LR	0.71	1.78	0.76	2.62	0.88	1.05	0.46	1.93
MIROC-ES2L	0.35	-0.16	-0.66	0.11	-0.79	-0.62	-0.64	0.2
MPI-ESM1-2-LR	0.3	0.55	0.34	1.22	0.15	0	0.48	0.72
UKESM1-0-LL	1.05	1.14	0.93	1.56	0.66	1	0.51	1.4
Multi-model mean	0.66	1	0.59	1.54	0.47	0.54	0.36	1.12

Supplementary Figures
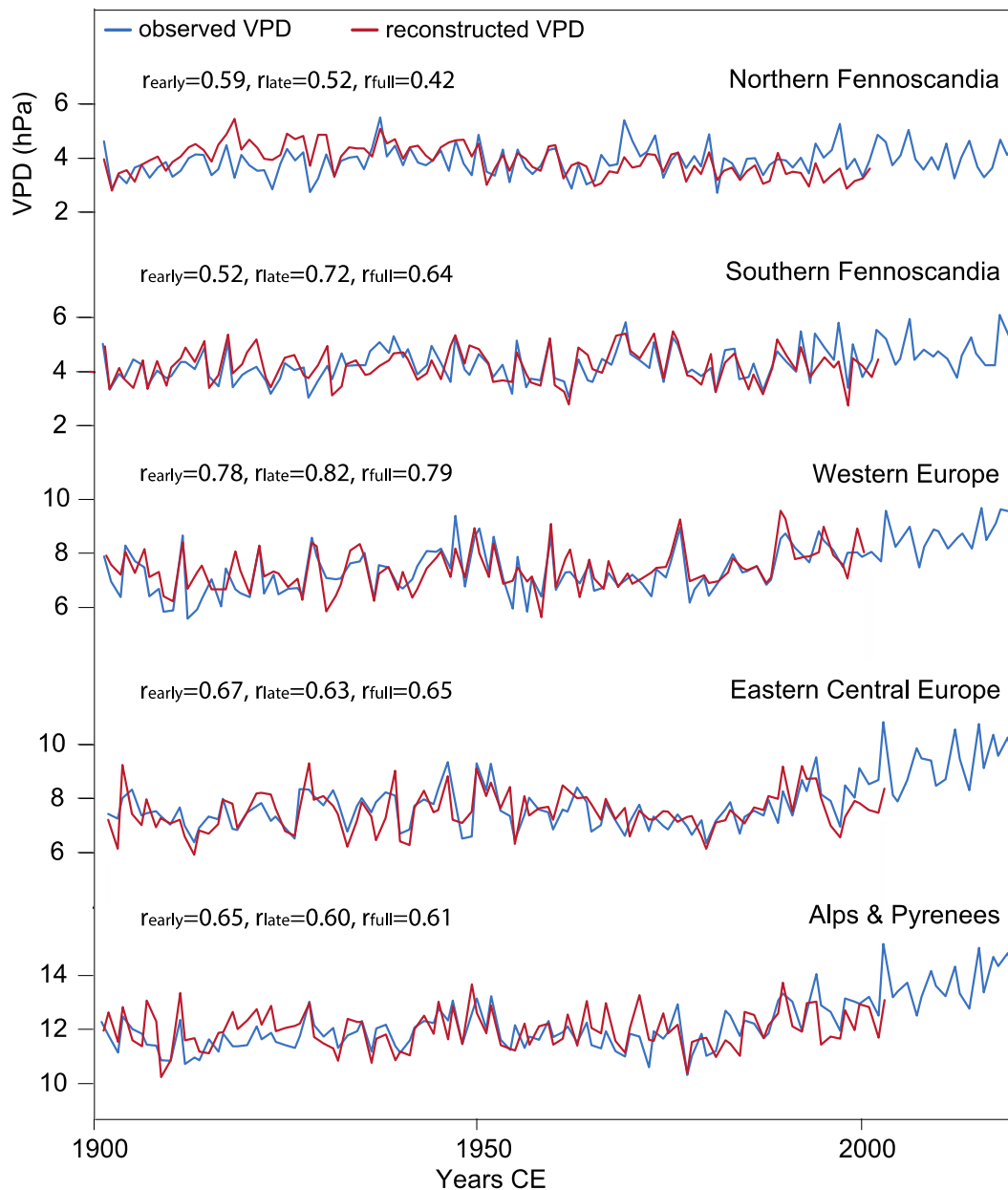
Supplementary Figure 1. Relationship between observed (blue) and reconstructed (red) Summer VPD (June-August) for the five European clusters. Calibration period 1920-2000; early period 1920-1960, late period 1961-2000. All correlation coefficients are significant at p<0.01. Despite highly significant correlation coefficients in NF, differences in the long-term trends between observed and reconstructed VPD together with non-robust calibration-verification statistics shown in Supplementary Table 3 hinder generating a robust reconstruction for this region.
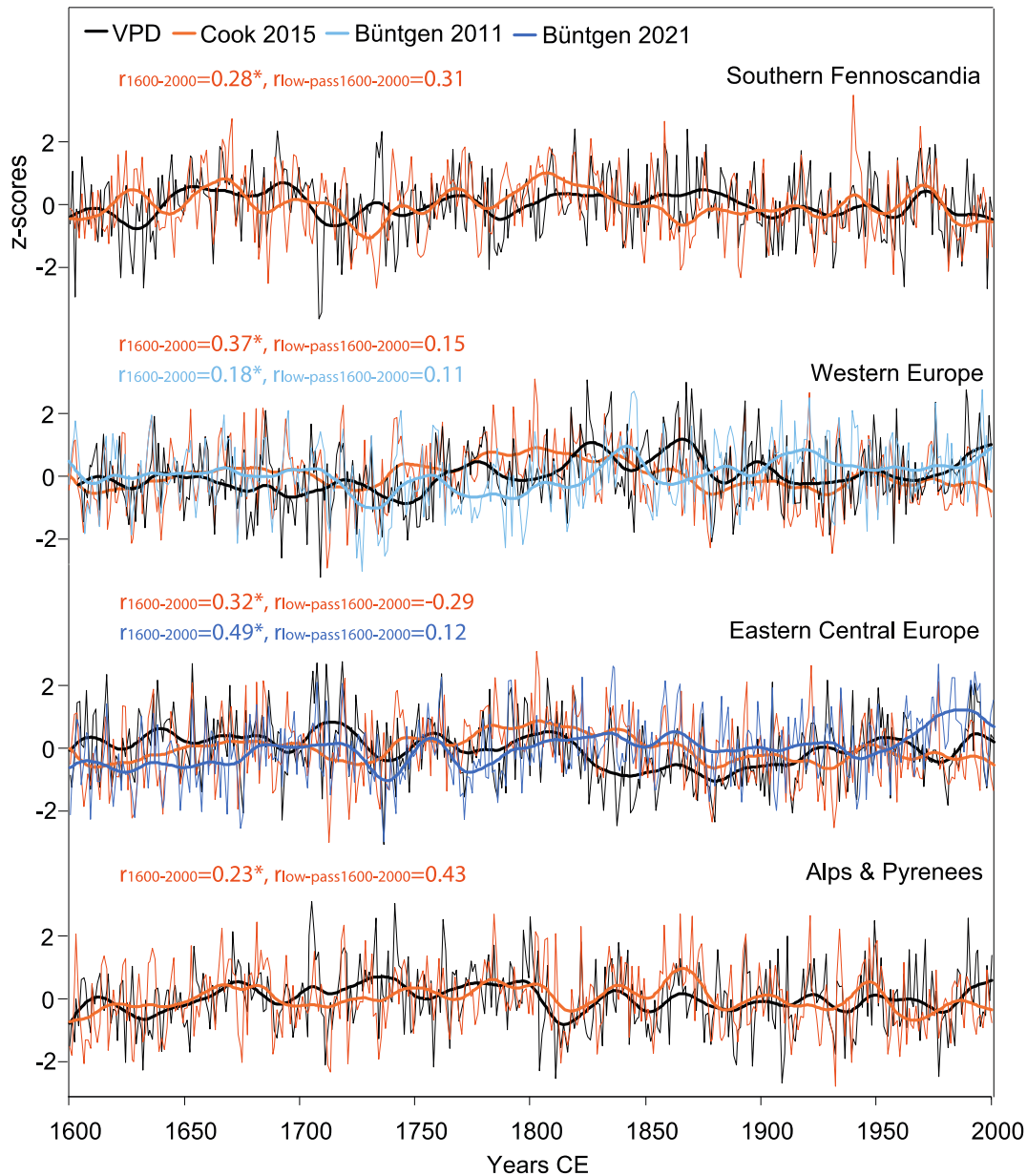
Supplementary Figure 2. Comparison of the four European summer VPD reconstructions to summer drought reconstructions (scPDSI) of Cook et al. (2015)[68], Büntgen et al. (2011)[69] (April-June precipitation Western Europe) and Büntgen et al. (2021)[70] (scPDSI, Eastern Central Europe). PDSI and precipitation reconstructions are displayed inversely for direct comparison with VPD (high values dry, low values moist). Regional gridpoint means of Cook et al. were extracted with the Climate Explorer (http:// climexp.knmi.nl/) for the areas corresponding to the areas of the VPD reconstructions: Southern Fennoscandia: 13.5-31.5 E, 60.0-63.0 N, Western Europe -3.0-3.5 E, 45.0-55.0 N; Eastern Central Europe: 16.0-25.5 E, 47.0-50.0 N, Alps&Pyrennes: mean of the regions 7.5-9.5 E, 46.5-47.5 N (Alps) and 1.0-2.0 E, 42.0-43.0 N (Pyrenees). Thick lines are 30-year smoothing splines, stars are Pearson's correlation coefficients significant at p<0.01. $r_{low-pass}$ indicate correlations between the 30-year splines.
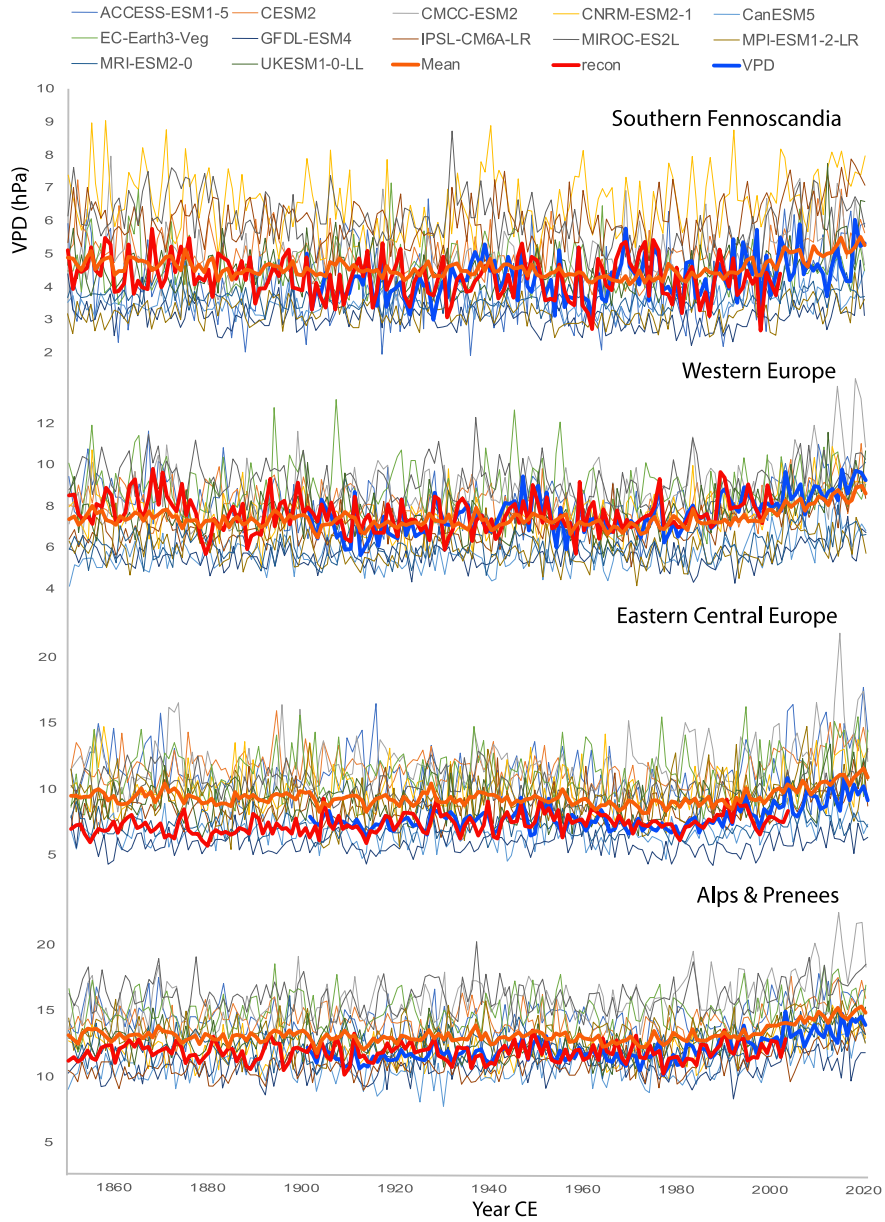
Supplementary Figure 3. Comparison of the time series of observed (thick blue line), reconstructed (thick red line) and multi-model mean (thick orange line) summer VPD variations together with the time series of the individual model outputs (thin colored lines) for four European regions. In general, observed, reconstructed and multi-model mean VPD time series represent similar VPD levels and long-term trends, but differ in their relative year-to-year variations.
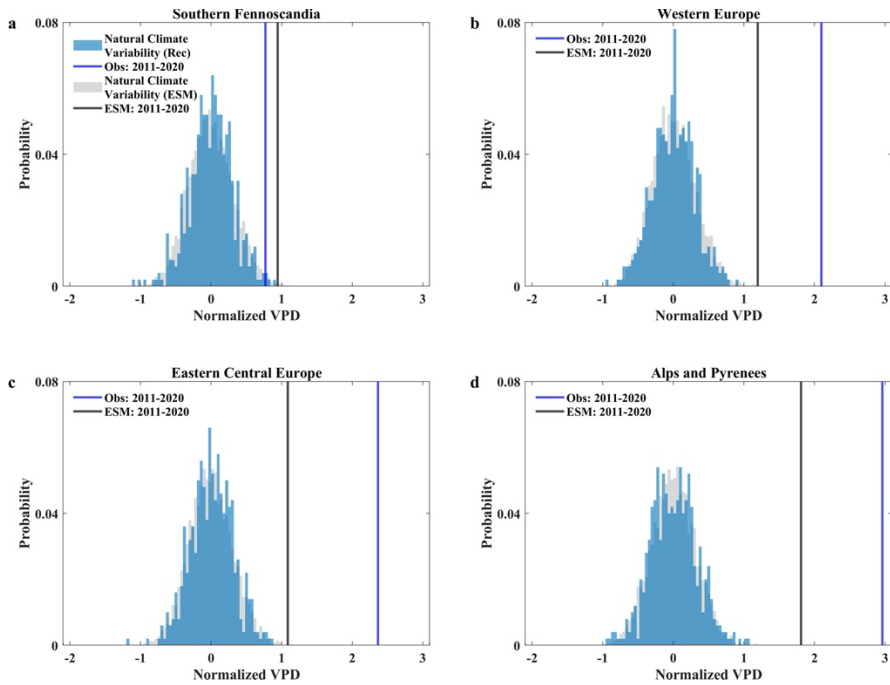
Supplementary Figure 4. Comparison of the estimated VPD variability of pre-industrial conditions to the recent average of VPD of the 10-year period 2011 to 2020 (instead of 1991-2020 as shown in Figure 4). Bars indicate pre-industrial natural variability from tree-ring $\delta^{18}O$-based VPD reconstructions for the period 1600-1850 (light blue), and from 500-year simulations of 12 ESMs with no human-induced forcing included, piControl scenario (grey). Pre-industrial variability was estimated from randomly sampled years of the simulations. Solid lines indicate VPD during the most recent climatic period 2011-2020 CE based on direct VPD observations (dark blue), the multi-model mean averaged VPD based on a combination of historical and ssp245 scenarios (black) (both include human-induced forcing). VPD values are normalized for comparability. Note that also for the most recent 10-year as for the 30-year period both observed and simulated summer VPD levels are unprecedented compared to pre-industrial conditions.
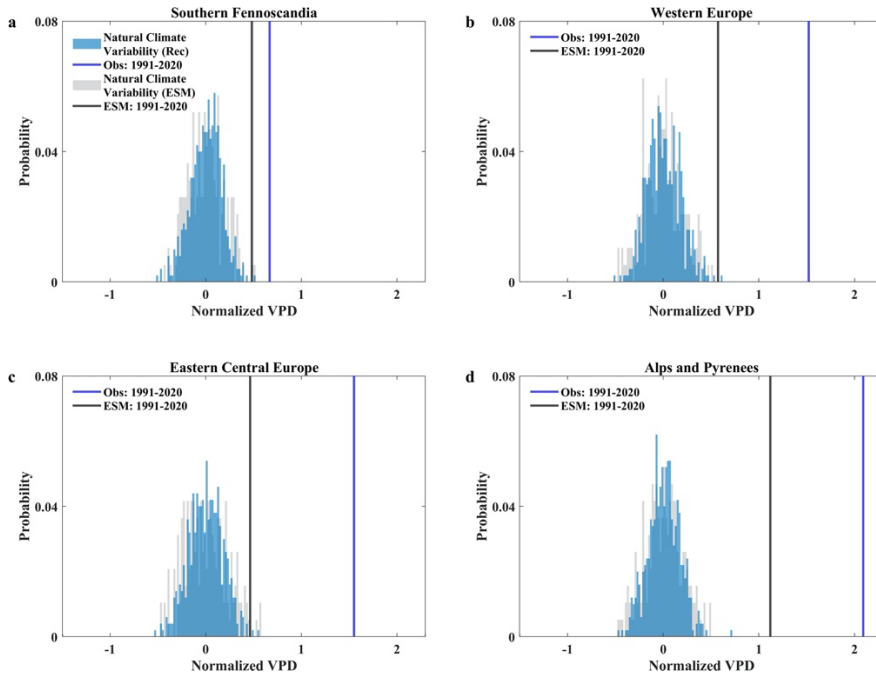
Supplementary Figure 5. Same as Figure S9 but for the 30-year period 1991-2020 and with pre-industrial variability estimated from consecutive non-overlapping periods of the simulations (instead of randomly sampled years as shown in Figure 4 and Figure S9). Note that when estimating pre-industrial variability from consecutive non-overlapping periods instead of randomly sampled years, both observed and simulated summer VPD levels remain unprecedented compared to pre-industrial conditions.